Journal Pre-proof

Full-spectrum responsive photocatalytic activity *via* non-noble metal Bi decorated mulberry-like $BiVO_4$

Yaxin Bi, Yanling Yang, Xiao-Lei Shi, Lei Feng, Xiaojiang Hou, Xiaohui Ye, Li Zhang, Guoquan Suo, Siyu Lu, Zhi-Gang Chen

PII: S1005-0302(21)00113-4

DOI: https://doi.org/10.1016/j.jmst.2020.11.079

Reference: JMST 2863

To appear in: *Journal of Materials Science & Technology*

Received Date: 15 September 2020

Revised Date: 28 November 2020

Accepted Date: 30 November 2020

Please cite this article as: Bi Y, Yang Y, Shi X-Lei, Feng L, Hou X, Ye X, Zhang L, Suo G, Lu S, Chen Z-Gang, Full-spectrum responsive photocatalytic activity *via* non-noble metal Bi decorated mulberry-like $BiVO_4$, *Journal of Materials Science and amp; Technology* (2021), doi: https://doi.org/10.1016/j.jmst.2020.11.079

Full-spectrum responsive photocatalytic activity *via* non-noble metal Bi decorated mulberry-like $BiVO_4$

Yaxin Bi[a,§], Yanling Yang[a,§,*], Xiao-Lei Shi[b,c,§], Lei Feng[a], Xiaojiang Hou[a], Xiaohui Ye[a], Li Zhang[a], Guoquan Suo[a], Siyu Lu[d], Zhi-Gang Chen[b,c,*]

[a] School of Materials Science and Engineering, Shaanxi Key Laboratory of Green Preparation and Functionalization for Inorganic Materials, Shaanxi University of Science and Technology, Xi'an 710021, China

[b] Centre for Future Materials, University of Southern Queensland, Springfield, QLD 4300, Australia

[c] School of Mechanical and Mining Engineering, The University of Queensland, Brisbane, QLD 4072, Australia

[d] College of Chemistry and Molecular Engineering, Zhengzhou University, Zhengzhou 450001, China

[§] These authors contribute equally to this work.

* Corresponding authors.

E-mail addresses: yangyanling@sust.edu.cn (Y.L. Yang); zhigang.chen@usq.edu.au (Z.G. Chen).

Graphical abstract

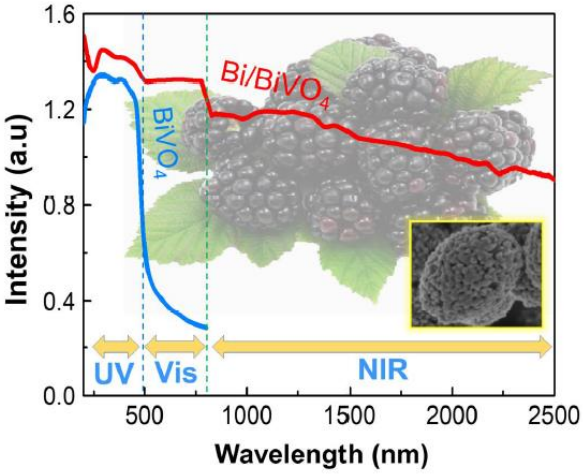

Highlight

- An *in-situ* synthesis method for non-noble metal Bi decorated mulberry-like $BiVO_4$;
- Bi/$BiVO_4$ exhibits full-spectrum (UV-Vis-NIR) responsive photocatalytic activities;
- Surface plasmon resonance effects of Bi and synergetic effects between Bi and $BiVO_4$.
- Density functional theory (DFT) calculation verify the electron transfer mechanism.

Abstract

Due to its appropriate bandgap (~2.4 eV) and efficient light absorption, bismuth vanadate ($BiVO_4$) shows promising photocatalysis activity. However, the charge carrier recombination and poor electron transmission often induce poor photocatalytic performance. Herein, we report a new method to *in-situ* synthesize non-noble metal Bi decorated mulberry-like $BiVO_4$ by a two-step calcination process. Comprehensive characterizations reveal that non-noble metal Bi nanoparticles grown *in-situ* on $BiVO_4$ result in the red-shift of the absorbance edge, greatly extending the light absorption from the ultraviolet into the near-infrared region. The surface plasmon resonance excitation of Bi nanoparticles and synergetic effects between Bi and $BiVO_4$ effectively improve the photocatalytic efficiency and promote the separation of

photoinduced electron-hole pairs in mulberry-like $BiVO_4$. Density functional theory (DFT) calculation results further verify that the electrons are transferred from Bi to $BiVO_4$ and the formation of •OH radical in Bi/$BiVO_4$ is attributed to the lower simulated free energy, which supports our experimental outcomes. This work provides a novel strategy to enhance light absorption and promote efficient solar utilization of photocatalysts for practical applications.

Key words: Bi; $BiVO_4$; Photocatalysis; Full-spectrum; Density functional theory

1. Introduction

As a typical environmental-friendly and renewable energy source, solar energy has drawn extensive attention in the past decades [1]. Owing to its non-toxic and highly active features, TiO_2 is a widely-used traditional photocatalyst. However, intrinsic TiO_2 is only active by ultraviolet light illumination [2], thus to develop a suitable and efficient alternative to TiO_2 is of significance. Recently, $BiVO_4$ with an appropriate bandgap of 2.4 eV has been regarded as a promising photocatalyst for using full-spectrum sunlight [3]. However, its limited quantum yield with no response to near-infrared (NIR) wavelengths restricts the photodegradation efficiency [4]. In this regard, it is critical to develop a new strategy to enhance the light response and inhibit the recombination efficiency of the photoinduced electron-hole pairs.

To achieve this goal, effective efforts such as introducing a small number of appropriate heteroatoms by doping have been performed [5], including N [6], F [7], and C [8]. For example, La/B co-doped $BiVO_4$ prepared by a sol-gel method with a high specific surface area contributed a higher methyl orange degradation rate of more than 98.4% [9], derived from the significant effects of heteroatoms, which narrow the bandgap and promote

the separation of charge carriers. However, the low solid solution and inhomogeneous distribution of heteroatoms cause challenges to extend strong visible-light absorption [10,11].

Loading metal particles is another efficient strategy to inhibit the formation of recombination centers of photo-generated electron-holes pairs, such as W [12], Tm [13], Ag [14], Mo [15], and Eu [16]. In addition, benefiting from the surface plasmon resonance (SPR) effect, noble metals have been applied to approach the superior photocatalytic activity of semiconductor photocatalysts. It was reported that Ag-decorated $BiVO_4$ photocatalyst was synthesized to improve charge separation efficiency with perfect photocatalytic activity than that of the pure $BiVO_4$ [17]. However, the addition of expensive and scarce metals on $BiVO_4$ severely limits the practical applications as photocatalysts because of the high cost [18].

Non-noble metal Bi is an ideal alternative for noble metals because of its metal-like SPR effect [19,20]. For instance, Bi nanoparticles have been combined with some semiconductor photocatalysts, such as $Bi_2O_2CO_3$ [21], Bi_2WO_6 [22], $BiPO_4$ [23], and BiOBr [24]. As a result of the SPR of Bi metal and effective charge separation, the construction of Bi metal-modified semiconductors possesses a higher photocatalytic performance than that of the individual materials alone. Besides, it is easy to accomplish the reduction process from Bi ion to Bi metal due to the electron capture ability and the large work function of Bi [25].

Bi-based composites can be prepared by various *in-situ* reduction strategies, including photo-reduction, chemical reduction, and hydrothermal reduction [26]. In this work, we originally *in-situ* synthesize non-noble metal Bi decorated mulberry-like $BiVO_4$ composites ($Bi/BiVO_4$) by a two-step calcination process in a controlled atmosphere with monoclinic $BiVO_4$ as the raw material. Benefiting from the noble-metal-like behavior of Bi and the synergetic effects between Bi and $BiVO_4$, the $Bi/BiVO_4$ composites show a substantial improvement in the light absorption, and provide a new strategy to tackle the problem of no response to near-infrared wavelengths.

2. Experimental details

2.1. Synthesis of Bi/$BiVO_4$ composites

The Bi/$BiVO_4$ composites were synthesized *via* a facile two-step calcination method. Firstly, 0.4 mmol $Bi(NO_3)_3 \cdot 5H_2O$ was dissolved in 16 mL of glycerol with stirring for 1 hour (h). Then, the same amount of $NaVO_3 \cdot 2H_2O$ was dissolved in another 16 mL of deionized water, and it can be clearly observed that it gradually transformed into transparent and homogeneous after stirring for 0.5 h at room temperature. Afterward, a yellowish suspension was formed by mixing the above two solutions under stirring. For a solvothermal process, the above solution was heated at 180 ℃ for 8 h. Subsequently, the powder was obtained *via* washing with deionized water and ethanol and afterward drying overnight in a vacuum oven at 60 ℃. The $BiVO_4$ precursor was obtained. Then, the precursor was transferred into a muffle furnace and calcined at 300 ℃ to make sure structural stability. After that, the product was calcined at 350 ℃ for 10 h with a heating rate of 5 ℃ min^{-1} in Ar/H_2 (95%:5%, vol.%) to obtain Bi/$BiVO_4$ composite.

2.2. Sample characterization

The microstructure and structural information of samples was analyzed by X-ray diffraction (XRD, D/Max-2200PC) and field emission scanning electron microscope (SEM, Hitachi S4600). The elemental analysis and microstructures of Bi/$BiVO_4$ were taken on energy-dispersive X-ray spectroscopy (EDS) and transmission electron microscopy (TEM, JEM-2100F) with an accelerating voltage of 200 kV. Raman spectra were measured on the Renishaw-invia Raman spectroscope. X-ray photoelectron spectroscopy (XPS, AXIS SUPRA) was used to characterize the chemical bonding states of Bi/$BiVO_4$. Optical spectra were obtained on a Cary 5000 spectrophotometer equipped with an integrating sphere and $BaSO_4$ as a reflectance standard. Photoluminescence (PL) spectra were examined using a fluorescence spectrophotometer (F-4500, Hitachi, Japan). The photocurrents and

electrochemical impedance spectroscopy (EIS) of Bi/$BiVO_4$ were obtained on a CHI660E electrochemical workstation at room temperature.

2.3. Photocatalytic activity test

Taking consideration into the practical applications, the sunlight covers ultraviolet, visible and near-infrared light (UV-vis-NIR), which can be widely used in actual production. On this regard, the photocatalytic performances of the prepared catalysts were determined by the degradation rate of Rhodamine B (RhB) and phenol under a simulated solar light, a 500 W Xenon lamp as light source. The absorbance of RhB and phenol were examined by a UV-vis detector (L5s). 20 mg of the powder sample was dispersed in 50 mL solution (10 mg L^{-1}). Before irradiation, the solution was stirred for 30 minutes (min) in darkness to achieve an adsorption-desorption equilibrium condition. At 20 min intervals, 4 mL of suspension was removed regularly and centrifuged to separate the photocatalyst. In order to weaken the heat generated by the lamp and reduce the thermal effect during photocatalytic degradation, the Xe lamp acts as light source and is equipped with cold trap, which is surrounded by circulating cooling water. Such a set-up aims to eliminate the effect of temperature shift on the photocatalytic activity. Then the concentration of RhB and phenol were measured by UV-vis detector.

The degradation efficiency (%) can be evaluated using the equation:

$$\text{Degradation efficency}\ (\%) = (C_0 - C)/C_0 \times 100\% \quad (1)$$

where C_0 represents the initial concentration of RhB and phenol , and C refers to the RhB and phenol concentration after irradiation for a certain duration [27].

2.4. Density functional theory calculation

The first-principles density functional theory (DFT) calculations are carried out with the projector augmented wave (PAW) method [28,29]. The exchange-functional is treated using

the generalized gradient approximation (GGA) of Perdew-Burke-Ernzerhof (PBE) [28] functional. The free energy was calculated using the equation [30]:

$$G = E + \mathrm{ZPE} - TS \quad (2)$$

where *G*, *E*, ZPE and *TS* are the free energy, total energy from DFT calculations, zero point energy and entropic contributions (Temperature was set to be 300 K), respectively.

3. Results and discussion

3.1. Material properties

To understand the microstructure and morphology of the pure $BiVO_4$ and $Bi/BiVO_4$, detailed SEM were performed, and the results are shown in Fig. 1(a) and (b). Fig. 1(c) illustrates that mulberry-like $Bi/BiVO_4$ can be formed after partial reduction of $BiVO_4$. $BiVO_4$ and $Bi/BiVO_4$ are assembled by many nanoparticles and have similar mulberry-like morphology. There is no significant morphological difference between pure $BiVO_4$ and $Bi/BiVO_4$, indicating that Bi grows *in-situ* on $BiVO_4$, and the generation of Bi has little effect on the morphology of $BiVO_4$. Such a growth process is governed by the Ostwald ripening process of microspheres [31], where the nanoparticles assemble at the primary stage of the solvothermal reaction, which is controlled by the nucleus to reduce surface energy. After 8 h of solvothermal process, irregular amorphous particles are stacked together to form the mulberry-like morphology. For photocatalysts, their activities are associated with the particle size. The larger crystal size can induce more surface recombination of photogenerated charge carriers. On the other hand, when the grain size reduces, the recombination rate decreases. Compared with the previous report [32], the mulberry-like $Bi/BiVO_4$ shows smaller diameters of ~400-600 nm and is assembled by numerous nanoparticles, which should have larger surface area and volume ratio, leading to a higher photocatalytic activity because nanoparticles with small size distribution may result in shorter distances of excited electrons

moving to the surface, which not only decreases carriers recombination but also enhances photocatalytic activity [33].

To further investigate the microstructure and morphology of the pure $BiVO_4$ and $Bi/BiVO_4$, TEM were performed, and the results are displayed in Fig. 1(d-g). As can be seen, the mulberry-like morphology is assembled by nanoparticles. As shown in Fig. 1(g), the lattice fringes of 0.47 nm and 0.23 nm are corresponding to the (101) facets of $BiVO_4$ (PDF. 75-1867) and the (110) facets of Bi (PDF. 85-1331), respectively. The TEM image of $Bi/BiVO_4$ further proves that non-noble metal Bi and monoclinic $BiVO_4$ coexist in composites, which is in consistence with the XRD results. Fig. 1(h) shows the EDS elemental mapping images of $Bi/BiVO_4$, indicating that O, V, and Bi are uniformly distributed.

To illustrate the composition and crystalline structures of the pure $BiVO_4$ and $Bi/BiVO_4$, XRD was used to analyze $BiVO_4$ and $Bi/BiVO_4$, and the results are shown in Fig. 2(a). The sharp and distinct peaks suggest the high purity and crystallinity of products. An intensive peak of $BiVO_4$ at ~33.7° could be well indexed to the (112) plane of phase-pure $BiVO_4$ crystallites (PDF 75-1867), which is consistent with monoclinic $BiVO_4$. In the case of $Bi/BiVO_4$, the peaks of the crystalline patterns of $BiVO_4$ and metallic Bi are co-existed, indicating that partial $BiVO_4$ was reduced to metallic Bi, and $Bi/BiVO_4$ composites were formed after the two-step calcination process. The formation of metallic Bi can be attributed to the *in-situ* reduction of Bi^{3+} profiting from the reduction effects of H_2. The content of Bi in $BiVO_4$ can be controlled by the reaction temperature, reaction time, and the Ar/H_2 atmosphere during calcination progress [34-37]. Because metallic Bi is easily oxidized under air, some weak peaks can be attributed to the formed thin layer of bismuth oxide, preventing the Bi metal from being further oxidized [38]. The two weak peaks at ~31.8° and ~32.8° are consistent with the Bi_7VO_{13} crystallites (PDF 44-0322), which is an intermediate product during hydrothermal progress and is not discussed here.

To quantitatively investigate the size of crystalline materials, the Scherrer equation was applied to estimate the grain size of as-synthesized Bi/$BiVO_4$ from the characteristic peaks in XRD pattern. The Scherrer equation can be expressed as follows:

$$D = \frac{\kappa\lambda}{\tau \cos\theta} \tag{3}$$

where D is the crystal size, λ is the X-ray wavelength, κ is a shape factor constant, τ is full width at half maximum, and θ is the Braggs angle [39]. As a result, the crystallite sizes of Bi/$BiVO_4$ determined by Scherrer equation are 40.3 nm for Bi and 29.1 nm for $BiVO_4$. The calculated results indicate that the mulberry-like morphology with diameters ranging from 400 to 600 nm is assembled by numerous Bi and $BiVO_4$ nanoparticles, consistent with the SEM results in Fig. 1(b).

The structure and bonding states of the pure $BiVO_4$ and Bi/$BiVO_4$ were characterized by Raman spectroscopy, and the results are presented in Fig. 2(b). The observed peaks centered at 137, 196, 332, and 817 cm^{-1} are in agreement with the Raman characteristics of monoclinic $BiVO_4$ [40]. The peak at 817 cm^{-1} is attributed to the asymmetric and symmetric V-O stretching mode. Compared with $BiVO_4$, the intensity of the peak centered at 817 cm^{-1} for Bi/$BiVO_4$ is significantly decreased, indicating the decrease of the V-O band. The decreased V-O band suggests that partial $BiVO_4$ was reduced to metallic Bi, in accordance with the XRD results. The band centered at 332 cm^{-1} is associated with the asymmetric and symmetric bending vibration, which is attributed to the VO_4 band. The peak centered at 196 cm^{-1} can be ascribed to the external mode of rotation and translation [41]. From the above Raman observation, it can be concluded that the non-noble metal Bi decorated mulberry-like $BiVO_4$ has been successfully *in-situ* synthesized by a two-step calcination process. Fig. 2(c) schematically illustrates this two-step calcination process, in which non-noble metal Bi is formed from $BiVO_4$ at the second calcination.

To explore the presence of various elements and the chemical states of the pure $BiVO_4$ and Bi/$BiVO_4$, XPS was further performed, and the results are shown in Fig. 3(a). Here, all data were adjusted in accordance with C 1s peak at 284.6 eV from adventitious carbon as a reference. Fig. 3(b-d) shows the slow-scanned XPS spectra of Bi 4f, V 2p and O 1s for the pure $BiVO_4$ and Bi/$BiVO_4$, respectively. In the fine spectrum of the Bi 4f region of $BiVO_4$, two peaks centered at ~158.59 eV and 163.89 eV correspond to Bi $4f_{7/2}$ and Bi $4f_{5/2}$ states of Bi^{3+} species, respectively, due to spin-orbital splitting [42]. The two peaks shift to centers at 158.76 and 164.05 eV for Bi/$BiVO_4$, respectively [38]. Besides, two weak peaks centered at ~157.14 eV and 162.67 eV can be detected and indexed as the feature of metallic Bi [19,38]. It is believed that peak shifts of Bi $4f_{7/2}$ and Bi $4f_{5/2}$ should be attributed to the interaction of non-noble metal Bi and $BiVO_4$ [43]. The fine spectrum of V in Fig. 3(c) contains two peaks centered at ~516.28 and 523.71 eV, which belong to V $2p_{3/2}$ and V $2p_{1/2}$ of V^{5+}, respectively. These two peaks shift to 516.59 and 524.1 eV in Bi/$BiVO_4$, respectively. The shifts of V 2p spectra are ascribed to the chemical environment change of V atoms, arising from the Bi defects [44]. For O 1s spectra (Fig. 3(d)), the peaks at 528.76 eV and 532.12 eV correspond to the lattice oxide (O_I) species and adsorbed oxygen (O_{II}) species. It is also observed that the binding energy centered at 530.6 eV belongs to the oxygen in the $BiVO_4$ lattice, which is shifted to 530.79 eV in the Bi/$BiVO_4$ composite photocatalysts [32]. On this basis, we suspect that the shifts of Bi/$BiVO_4$ in XPS spectra may be attributed to the surface Bi defects. Similar phenomena were also observed in the previous reports [32,45]. Fig. 3(e) shows the Fourier transform infrared (FTIR) spectra of $BiVO_4$ and Bi/$BiVO_4$. For monoclinic $BiVO_4$ and Bi/$BiVO_4$, the vibrational peak centered at 739 cm^{-1} can be observed, which is indicative of asymmetric stretching vibration of the ν_3 (VO_4) [46]. The particle morphology and size distributions of the non-noble metal Bi modified mulberry-like $BiVO_4$ are shown in Fig. 3(f), indicating that the catalysts present regular refined particles. The inset of Fig. 3(f) shows the

distribution of particle diameters, from which the particles are agglomerated with an average size of ~540 nm.

To illustrate the optical absorption properties of $BiVO_4$ and $Bi/BiVO_4$, UV-vis absorption spectroscopy was performed, and the results are shown in Fig. 4(a). As can be seen, $Bi/BiVO_4$ has much higher absorption efficiency in UV-vis-NIR region. The absorption edge of $BiVO_4$ was located at ~500 nm. In comparison with $BiVO_4$, the photo-response of $Bi/BiVO_4$ increases to the NIR region after the *in-situ* generation of Bi nanoparticles. Moreover, the photo-response of $Bi/BiVO_4$ increases to a considerable extent in UV and visible region. The intense and extensive absorptions are larger than 500 nm, which should derive from the strong SPR effect of the non-noble metallic Bi nanoparticles [47]. Meanwhile, the high absorption intensity of $Bi/BiVO_4$ in NIR region is observed, which should be attributed to the interaction of metallic Bi and $BiVO_4$. Such phenomena should be beneficial to the photocatalytic activity, which is similar to the reported result [48]. On the basis of the formula [49]:

$$\alpha h\upsilon = A(h\upsilon - E_g)^{n/2} \quad (4)$$

where α is the absorption coefficient, h is the Planck constant, υ is the light frequency, and A is the proportionality constant, respectively. Here, the n value is 1 for direct-gap semiconductor and 4 for indirect-gap semiconductor, the bandgap (E_g) for $BiVO_4$ and $Bi/BiVO_4$ can be estimated to be 2.45 and 1.90 eV, as shown in Fig. 4(b).

The valence band (VB) and conduction band (CB) potentials can be determined by the following equations [26,50]:

$$E_{CB} = X - E_e - E_g/2 \quad (5)$$

$$E_{VB} = E_{CB} + E_g \quad (6)$$

where X is the electronegativity of the semiconductor, E_{VB} is the valence band potential, E_{CB} is the conduction band potential, and E_e is the energy of free electrons on the hydrogen scale

about 4.5 V, respectively. Besides, the position of E_{VB} of $BiVO_4$ is +2.81 eV. According to the above equations, the position of E_{CB} can be calculated to be +0.36 eV.

To investigate the separation efficiency of photogenerated electron-hole pairs, the PL spectra of the pure $BiVO_4$ and $Bi/BiVO_4$ is performed, and the results are shown in Fig. 4(c). It is well-known that weaker PL intensity represents a lower recombination rate [51]. Compared with that of $BiVO_4$, the emission peak intensity of $Bi/BiVO_4$ is considerably diminished, implying the lower recombination rate of electron-hole pairs. This should be ascribed to the SPR effect of metallic Bi, which can restrain the recombination of photo-generated electrons and holes [52].

3.2. Photocatalytic properties and stability

To evaluate the photocatalytic properties of $BiVO_4$ and $Bi/BiVO_4$, RhB degradation efficiencies under the same conditions were measured, and the results are shown in Fig. 4(d). For comparison, the experiment on direct photolysis of RhB was also conducted under the same conditions. Apparently, the RhB conversion is quite lower after 120 min, confirming that the direct photolysis of RhB can be negligible. Similarly, the photocatalysis without light of the samples can be negligible. As can be seen, pure $BiVO_4$ displays relatively poor degradation efficiency. Also, when $BiVO_4$ interacts with Bi, the RhB degradation rate of $Bi/BiVO_4$ is obviously increased. Notably, $Bi/BiVO_4$ shows the highest RhB degradation ability of 80.9% within 120 min irradiation, exceeding that of the pure $BiVO_4$ (13.6%) by a factor of 6 (Fig. 4(e)). In addition, the photocatalytic activity of $Bi/BiVO_4$ was also detected by phenol degradation under simulated sunlight irradiation. Owing to the stability of phenol, the adsorption and conversion of phenol can be negligible without photocatalysts during the photocatalytic process. The degradation ratios for the phenol dye of pure $BiVO_4$ and $Bi/BiVO_4$ in 180 min are exhibited in Fig. 4(h). Apparently, the $Bi/BiVO_4$ shows an enhanced photocatalytic efficiency of 73.3% compared to the pure $BiVO_4$ (17.1%). The

results further reveal that the constructed Bi/$BiVO_4$ composite photocatalyst displays enhanced photocatalytic performance due to the SPR of Bi. Meanwhile, the synergistic effect of Bi and $BiVO_4$ can prevent the photogenerated electron and holes from recombining, and play a crucial role in the enhanced photocatalytic activity [53]. To confirm the photochemical stability of Bi/$BiVO_4$, the catalytic recycling experiments in the photodegradation of RhB were performed and the results are plotted in Fig 4(f). After testing more than five times, the performance of Bi/$BiVO_4$ only shows a slight decrease, illustrating its convenient reuse and excellent stability, which is particularly significant for its practical application.

To further investigate the degradation kinetics, the variations in $\ln(C/C_0)$ as a function of reaction time are calculated, and the results are shown in Fig. 4(g) and (i). The pseudo-first-order kinetic equation is given by [54]:

$$\ln(C/C_0) = -k_a t \quad (7)$$

where C is the concentration of RhB and phenol at time t, C_0 is the initial RhB and phenol concentration before irradiation, and k_a is the first-order apparent rate constant. The rate constants and relative coefficients (R^2) were presented in Table 1. The linear relation demonstrates that the photocatalytic reaction can be regarded as a pseudo-first-order reaction. Obviously, the kinetic constant of Bi/$BiVO_4$ is faster than that of pure $BiVO_4$, which further confirms that the SPR effect of non-noble metallic Bi and the synergistic effect between $BiVO_4$ and Bi can benefit the photocatalytic activity.

3.3. Electrochemical properties

To further analyze the enhanced charge transfer and separation efficiency in pure $BiVO_4$ and Bi/$BiVO_4$, electrochemical impedance spectroscopy (EIS) was performed, and the results are plotted in Fig. 5(a). The transfer resistance of surface charge during redox reaction is measured by the arc radius in EIS spectroscopy. A smaller radius in a high-frequency region represents a lower impedance and a higher efficiency of charge transfer [55]. The impedance

arc radius of Bi/$BiVO_4$ is obviously smaller in comparison with $BiVO_4$, indicating that more electrons across the electrolyte interface in Bi/$BiVO_4$. The SPR effect of semimetal Bi would be beneficial for promoting the storage and shuttle of electrons. Therefore, the transfer efficiency of the charge carriers in Bi/$BiVO_4$ can be effectively enhanced. The equivalent electrical circuit is inserted and the corresponding values were computed by Zview software, listed in Table 2. The R_s, R_{ct}, CPE and W_1 can be interpreted as the overall electrolyte resistance, the charge transfer resistance, the constant phase element and the Warburg impedance, respectively [3]. As shown in Table 2, the R_{ct} value for Bi/$BiVO_4$ (10.87 Ω) is smaller than that of $BiVO_4$ (18.36 Ω), suggesting the less charge transfer resistance and the rapid electron transportation. This demonstrates that the SPR excitation of Bi nanoparticles and the synergistic effects between $BiVO_4$ and Bi can promote the charge transformation, thus enhancing its electrical conductivity. These results can be further affirmed *via* photocurrent responses of $BiVO_4$ and Bi/$BiVO_4$, as shown in Fig. 5(b). At a given potential, the working electrode of Bi/$BiVO_4$ exhibits much higher photocurrent density than that of pure $BiVO_4$. Moreover, during the five repeated on/off light cycles, the photocurrent remains stable. Through comparison of these two different results, it is obvious that the semimetal Bi *in-situ* grown on the surface of $BiVO_4$ plays a crucial role in generating photocurrent density profiting from the SPR effect [56].

3.4. Enhanced full-spectrum responsive activity

Although some $BiVO_4$-based catalysts have been studied [13,17,44,57-65], our work shows the expanding light response range, as summarized in Fig. 5(c). As can be seen, most of the reported Bi/$BiVO_4$ catalysts aim to improve degradation efficiency, and their light response ranges were ~400-600 nm with less response to near-infrared wavelength. In contrast, we achieve an enhanced full-spectrum responsive photocatalytic activity of non-noble metal Bi decorated mulberry-like $BiVO_4$. The results indicate that the photo-response

of Bi/$BiVO_4$ extends from UV to visible and then to the NIR with absorption intensity above 1 when Bi *in-situ* grows on $BiVO_4$ through two-step calcination. Such unique light absorption is attributed to the strong SPR effect of non-noble metallic Bi nanoparticles and the interaction of metallic Bi and $BiVO_4$, which is also conducive to the degradation rate, as shown in Fig. 5(d) that compared to reported works [66-73].

3.5. Mechanism of photocatalytic performance

3.5.1. Photocatalytic mechanism

According to the above analysis, Fig. 6 schematically illustrates the possible photocatalytic mechanism of charge separation and transportation in Bi/$BiVO_4$. Under the solar-simulated light irradiation, the electrons on the VB can be excited to the CB of Bi/$BiVO_4$ by the high energy photon, and the equal photogenerated holes are generated. Meanwhile, the SPR of non-noble metallic Bi is excited, promoting the charge separation and transfer at the $BiVO_4$ interface [74]. Bi acts as the activation sites for reactants activation [38] and the photoinduced electrons are easily transferred from Bi to $BiVO_4$ through the interface [75]. The enhanced photocatalytic properties of $BiVO_4$ result from the integration of the plasmonic component through plasmonic sensitization. h^+ can also easily oxidize pollutant with high potential and oxidize OH^- to •OH [76]. The photogenerated electrons and electrons transferred to $BiVO_4$ reduce O_2 to H_2O_2 [77]. Then, H_2O_2 captures an electron to form •OH radicals, while the •OH with high oxidation ability can oxidize pollutant [38].

3.5.2. Electron transfer mechanism and the formation of •OH radical

To build up the insight into the electron transfer mechanism of Bi/$BiVO_4$ during the photocatalytic process, DFT calculations were performed by using the GGA-PBE method. Fig. 7(a-d) illustrates the calculated structure and the corresponding energy band of Bi and $BiVO_4$ [78]. It can be observed that the CB bottom and VB top of $BiVO_4$ are located between the symmetry point of P and N, which belongs to the indirect band gap semiconductor [79].

When the Fermi level is set to be zero, the band gaps of Bi and $BiVO_4$ are ~0.9 eV and 2.5 eV. From Fig. 4(b), the experimental energy band gap can be determined to be 2.45 eV. Obviously, the simulated value is close to the experimental value, which is similar to the previous report [64].

To clearly analyze their band structures and hybridization states, the partial density of states (PDOS) between -5 eV and 5 eV for V, O and Bi atoms of Bi and $BiVO_4$ are simulated and plotted in Fig. 7(e) and (f). As a reference, the Fermi level is assigned the value of zero. By analyzing the PDOS of $BiVO_4$, we notice that the valence band maximum (VBM) is primarily occupied by O 2p states [80]. There are also some hybridizations with Bi 6p and V 3d states in the CBM, resulting in the V-O and Bi-O bond. Thus, the conduction band minimum (CBM) is predominantly dominated by V 3d states, including some hybridization with Bi 6p and O 2p orbitals [64].

Fig. 8(a) and (b) shows the calculated structure and band position of Bi/$BiVO_4$. It is well known that the electrons transfer from the high to low energy level. As shown in Fig. 8(b), the positions of the CB bottom and the VB top are both higher than that of $BiVO_4$. Therefore, the charge transfer easily occurs from Bi to $BiVO_4$ through the interface, further supporting the previous mechanism analysis as discussed in Fig. 6 [38,81]. When the photocatalyst absorbs the energy under the solar-simulated light irradiation, the electrons on the VB are excited to the CB and the holes should be left at the same time. Moreover, the photoinduced electrons of Bi are injected into the CB of $BiVO_4$ *via* the interface, according to the band gap positions. The metallic Bi can effectively accept partial electrons of $BiVO_4$ in VB before turning back to its original state, which is similar to that of Ag [34]. The transfer can sufficiently separate the electron-hole pairs and effectively prolong the lifetime of the carriers in $BiVO_4$. Meanwhile, the SPR of non-noble metallic Bi happens during the photocatalytic process, facilitating the charge separation and transfer [82]. The oxidation of

pollutant and OH^- occurs at the VB, attributed to the presence of h^+, while the conversion of O_2, H_2O_2 and •OH radicals occurs at the CB. Their free energy and corresponding structure during the conversion progress are exhibited in Fig. 8(c). It can be seen that compared with pure $BiVO_4$, the simulated free energy of $Bi/BiVO_4$ is obviously smaller, which is beneficial to promote the reaction [38]. Therefore, the $Bi/BiVO_4$ not only efficiently inhibits recombination of electron-hole pairs and promotes the separation of charge carriers, but also enhances the photocatalytic activity. Taking consideration into the above results, it can be concluded that $Bi/BiVO_4$ exhibits an enhanced performance profiting from the improved separation efficiency and the SPR effect of non-noble metallic Bi [83].

4. Conclusion

In summary, non-noble metal Bi decorated mulberry-like $BiVO_4$ photocatalysts are *in-situ* fabricated by two-step calcination. The as-grown Bi nanoparticles on $BiVO_4$ lead to the red-shift of the absorbance edge, which significantly extends the light absorption from UV into NIR. Their photocatalytic efficiency is considerably improved by the surface plasmon resonance excitation of the Bi nanoparticles and the synergetic effects between Bi and $BiVO_4$, and the separation of photo-induced electron-hole pairs in mulberry-like $BiVO_4$ is also obviously promoted. Our DFT calculation results further confirm that the electrons transfer easily from Bi to $BiVO_4$ *via* the interface and the remained holes accelerate the separation of carriers. Moreover, the lower simulated free energy of $Bi/BiVO_4$ contributes to the formation of •OH. This work paves a new way to boost the light absorption, and promote efficient solar utilization of photocatalysts for the practical applications.

Declaration of interests

The authors declare that they have no known competing financial interests or personal relationships that could have appeared to influence the work reported in this paper.

Acknowledgements

This work was financially supported by the National Natural Science Foundation of China (Nos. 51464020, 51704188, 51802181, 61705125 and 51702199) and Australian Research Council.

References

[1] X. Hong, Y. Kang, C. Zhen, X. Kang, L.C. Yin, J.T.S. Irvine, L. Wang, G. Liu, H.M. Cheng, Sci. China Mater. 61 (2018) 831-838.

[2] M. Xing, J. Zhang, F. Chen, Appl. Catal. B: Environ. 89 (2009) 563-569.

[3] S. Chen, D. Huang, G. Zeng, W. Xue, L. Lei, P. Xu, R. Deng, J. Li, M. Cheng, Chem. Eng. J. 382 (2020) 122840.

[4] C.A. Unsworth, B. Coulson, V. Chechik, R.E. Douthwaite, J. Catal. 354 (2017) 152-159.

[5] R. Asahi, T. Morikawa, T. Ohwaki, K. Aoki, Y. Taga, Science 293 (2001) 269.

[6] M. Wang, Q. Liu, Y. Che, L. Zhang, D. Zhang, J. Alloys Compd. 548 (2013) 70-76.

[7] J.Q. Li, Z.Y. Guo, H. Liu, J. Du, Z.F. Zhu, J. Alloys Compd. 581 (2013) 40-45.

[8] C. Yin, S. Zhu, Z. Chen, W. Zhang, J. Gu, D. Zhang, J. Mater. Chem. A 1 (2013) 8367-8378.

[9] M. Wang, Y. Che, C. Niu, M. Dang, D. Dong, J. Rare Earths 31 (2013) 878-884.

[10] G. Liu, L. Wang, C. Sun, X. Yan, X. Wang, Z. Chen, S.C. Smith, H.M. Cheng, G.Q. Lu, Chem. Mater. 21 (2009) 1266-1274.

[11] G. Liu, L.C. Yin, J. Wang, P. Niu, C. Zhen, Y. Xie, H.M. Cheng, Energy Environ. Sci. 5 (2012) 9603-9610.

[12] Y. Jia, Z. Wang, Y. Ma, J. Liu, W. Shi, Y. Lin, X. Hu, K. Zhang, Electrochim. Acta 300 (2019) 138-144.

[13] S. Ullah, E.P. Ferreira-Neto, C. Hazra, R. Parveen, H.D. Rojas-Mantilla, M.L. Calegaro, Y.E. Serge-Correales, U.P. Rodrigues-Filho, S.J.L. Ribeiro, Appl. Catal. B: Environ. 243 (2019) 121-135.

[14] Y. Chen, W. Huang, D. He, Y. Situ, H. Huang, ACS Appl. Mater. Interfaces 6 (2014) 14405-14414.

[15] V. Pasumarthi, T. Liu, M. Dupuis, C. Li, J. Mater. Chem. A 7 (2019) 3054-3065.

[16] Y. Zhang, M. Wang, G. Yang, Y. Qi, T. Chai, S. Li, T. Zhu, Sep. Purif. Technol. 202 (2018) 335-344.

[17] Y. Deng, L. Tang, C. Feng, G. Zeng, J. Wang, Y. Zhou, Y. Liu, B. Peng, H. Feng, J. Hazard. Mater. 344 (2018) 758-769.

[18] Y. Huang, H. Li, M.S. Balogun, W. Liu, Y. Tong, X. Lu, H. Ji, ACS Appl. Mater. Interfaces 6 (2014) 22920-22927.

[19] Z. Zhao, W. Zhang, Y. Sun, J. Yu, Y. Zhang, H. Wang, F. Dong, Z. Wu, Bi J. Phys. Chem. C 120 (2016) 11889-11898.

[20] Z.G. Chen, X. Shi, L.D. Zhao, J. Zou, Prog. Mater Sci. 97 (2018) 283-346.

[21] F. Dong, Q. Li, Y. Sun, W.K. Ho, ACS Catal. 4 (2014) 4341-4350.

[22] J. Jia, P. Xue, R. Wang, X. Bai, X. Hu, J. Fan, E. Liu, J. Chem. Technol. Biotechnol. 93 (2018) 2988-2999.

[23] J. Li, W. Zhang, M. Ran, Y. Sun, H. Huang, F. Dong, Appl. Catal. B: Environ. 243 (2019) 313-321.

[24] Y. Guo, Y. Zhang, N. Tian, H. Huang, ACS Sustain. Chem. Eng. 4 (2016) 4003-4012.

[25] Y. Sun, Z. Zhao, F. Dong, W. Zhang, Phys. Chem. Chem. Phys. 17 (2015) 10383-10390.

[26] X.L. Shi, X. Tao, J. Zou, Z.G. Chen, Adv. Sci. 7 (2020) 1902923.

[27] J. Li, Y. Xie, Y. Zhong, Y. Hu, J. Mater. Chem. A 3 (2015) 5474-5481.

[28] J.P. Perdew, K. Burke, M. Ernzerhof, Phys. Rev. Lett. 77 (1996) 3865.

[29] G.K.D. Joubert, Phys. Rev. B 59 (1999) 1758.

[30] J.K. Nørskov, T. Bligaard, A. Logadottir, J.R. Kitchin, J.G. Chen, S. Pandelov, U. Stimming, J. Electrochem. Soc. 152 (2005) J23.

[31] X.W. Lou, L.A. Archer, Z. Yang, Adv. Mater. 20 (2008) 3987-4019.

[32] Q. Jing, X. Feng, J. Pan, L. Chen, Y. Liu, Dalton Trans. 47 (2018) 2602-2609.

[33] A. Malathi, J. Madhavan, M. Ashokkumar, P. Arunachalam, Appl. Catal. A-Gen. 555 (2018) 47-74.

[34] Q. Wang, J. He, Y. Shi, S. Zhang, T. Niu, H. She, Y. Bi, Chem. Eng. J. 326 (2017) 411-418.

[35] Y. Lan, Z. Li, D. Li, W. Xie, G. Yan, S. Guo, Chem. Eng. J. 392 (2020) 123686.

[36] P. Jiménez-Calvo, C. Marchal, T. Cottineau, V. Caps, V. Keller, J. Mater. Chem. A 7 (2019) 14849-14863.

[37] Q. Hao, R. Wang, H. Lu, C.a. Xie, W. Ao, D. Chen, C. Ma, W. Yao, Y. Zhu, Appl. Catal. B: Environ. 219 (2017) 63-72.

[38] P. Chen, H. Liu, Y. Sun, J. Li, W. Cui, L.a. Wang, W. Zhang, X. Yuan, Z. Wang, Y. Zhang, F. Dong, Appl. Catal. B: Environ. 264 (2020) 118545.

[39] U. Holzwarth, N. Gibson, Nat. Nanotechnol. 6 (2011) 534.

[40] A. Galembeck, O.L. Alves, Thin Solid Films 365 (2000) 90-93.

[41] F.D. Hardcastle, I.E. Wachs, H. Eckert, D.A. Jefferson, J. Solid State Chem. 90 (1991) 194-210.

[42] J. Wang, Z. Zhang, X. Wang, Y. Shen, Y. Guo, P.K. Wong, R. Bai, Chin. J. Catal. 39 (2018) 1792-1803.

[43] A. Adenle, D.K. Ma, D.P. Qu, W. Chen, S. Huang, CrystEngComm 19 (2017) 6305-6313.

[44] D.K. Ma, M.L. Guan, S.S. Liu, Y.Q. Zhang, C.W. Zhang, Y.X. He, S.M. Huang, Dalton Trans. 41 (2012) 5581-5586.

[45] J. Wang, W. Jiang, D. Liu, Z. Wei, Y. Zhu, Appl. Catal. B: Environ. 176-177 (2015) 306-314.

[46] R.L. Frost, D.A. Henry, M.L. Weier, W. Martens, J. Raman Spectrosc. 37 (2006) 722-732.

[47] Z. Wang, C. Jiang, R. Huang, H. Peng, X. Tang, J. Phys. Chem. C 118 (2014) 1155-1160.

[48] Y. Yu, C. Cao, H. Liu, P. Li, F. Wei, Y. Jiang, W. Song, J. Mater. Chem. A 2 (2014) 1677-1681.

[49] K.L. Zhang, C.M. Liu, F.Q. Huang, C. Zheng, W.D. Wang, Appl. Catal. B: Environ. 68 (2006) 125-129.

[50] M.L. Guan, D.K. Ma, S.W. Hu, Y.J. Chen, S.M. Huang, Inorg. Chem. 50 (2011) 800-805.

[51] J. Cao, B. Xu, B. Luo, H. Lin, S. Chen, Catal. Commun. 13 (2011) 63-68.

[52] C.C. Shen, Q. Zhu, Z.W. Zhao, T. Wen, X. Wang, A.W. Xu, J. Mater. Chem. A 3 (2015) 14661-14668.

[53] S. Weng, B. Chen, L. Xie, Z. Zheng, P. Liu, J. Mater. Chem. A 1 (2013) 3068-3075.

[54] K.H. Ye, Z. Chai, J. Gu, X. Yu, C. Zhao, Y. Zhang, W. Mai, Nano Energy 18 (2015) 222-231.

[55] J.L. Song, X. Wang, C.C. Wong, Electrochim. Acta 173 (2015) 834-838.

[56] H.J. Chen, Y.L. Yang, M. Hong, J.G. Chen, G.Q. Suo, X.J. Hou, L. Feng, Z.G. Chen, Sustain. Mater. Technol. 21 (2019) e00105.

[57] Y. Wang, G. Tan, T. Liu, Y. Su, H. Ren, X. Zhang, A. Xia, L. Lv, Y. Liu, Appl. Catal. B: Environ. 234 (2018) 37-49.

[58] Y. Zhu, M.W. Shah, C. Wang, Appl. Catal. B: Environ. 203 (2017) 526-532.

[59] F. Chen, Q. Yang, Y. Wang, J. Zhao, D. Wang, X. Li, Z. Guo, H. Wang, Y. Deng, C. Niu, G. Zeng, Appl. Catal. B: Environ. 205 (2017) 133-147.

[60] S. Bao, Q. Wu, S. Chang, B. Tian, J. Zhang, Catal. Sci. Technol. 7 (2017) 124-132.

[61] J. Zhang, Y. Lu, L. Ge, C. Han, Y. Li, Y. Gao, S. Li, H. Xu, Appl. Catal. B: Environ. 204 (2017) 385-393.

[62] F.Q. Zhou, J.C. Fan, Q.J. Xu, Y.L. Min, Appl. Catal. B: Environ. 201 (2017) 77-83.

[63] F. Chen, Q. Yang, X. Li, G. Zeng, D. Wang, C. Niu, J. Zhao, H. An, T. Xie, Y. Deng, Appl. Catal. B: Environ. 200 (2017) 330-342.

[64] J. Zhang, F. Ren, M. Deng, Y. Wang, Phys. Chem. Chem. Phys. 17 (2015) 10218-10226.

[65] C. Li, S. Wang, T. Wang, Y. Wei, P. Zhang, J. Gong, Small 10 (2014) 2782-2782.

[66] T. Liu, G. Tan, C. Zhao, C. Xu, Y. Su, Y. Wang, H. Ren, A. Xia, D. Shao, S. Yan, Appl. Catal. B: Environ. 213 (2017) 87-96.

[67] C. Regmi, Y.K. Kshetri, T.H. Kim, R.P. Pandey, S.W. Lee, Mol. Catal. 432 (2017) 220-231.

[68] Y. Geng, P. Zhang, N. Li, Z. Sun, J. Alloys Compd. 651 (2015) 744-748.

[69] Z. Liu, Q. Lu, C. Wang, J. Liu, G. Liu, J. Alloys Compd. 651 (2015) 29-33.

[70] Y. Lu, Y.S. Luo, H.M. Xiao, S.Y. Fu, CrystEngComm 16 (2014) 6059-6065.

[71] U.M. García-Pérez, A. Martínez-de la Cruz, S. Sepúlveda-Guzmán, J. Peral, Ceram. Int. 40 (2014) 4631-4638.

[72] S. Chaiwichian, B. Inceesungvorn, K. Wetchakun, S. Phanichphant, W. Kangwansupamonkon, N. Wetchakun, Mater. Res. Bull. 54 (2014) 28-33.

[73] K. Natarajan, H.C. Bajaj, R.J. Tayade, Sol. Energy 148 (2017) 87-97.

[74] C. Zheng, C. Cao, Z. Ali, Phys. Chem. Chem. Phys. 17 (2015) 13347-13354.

[75] M. Sun, W. Zhang, Y. Sun, Y. Zhang, F. Dong, Chin. J. Catal. 40 (2019) 826-836.

[76] H. Huang, X. Han, X. Li, S. Wang, P.K. Chu, Y. Zhang, ACS Appl. Mater. Interfaces 7 (2015) 482-492.

[77] H. Huang, S. Tu, C. Zeng, T. Zhang, A.H. Reshak, Y. Zhang, Angew. Chem. Int. Ed. 56 (2017) 11860-11864.

[78] L. Hao, L. Kang, H. Huang, L. Ye, K. Han, S. Yang, H. Yu, M. Batmunkh, Y. Zhang, T. Ma, Adv. Mater. 31 (2019) 1900546.

[79] M. Li, S. Yu, H. Huang, X. Li, Y. Feng, C. Wang, Y. Wang, T. Ma, L. Guo, Y. Zhang, Angew. Chem.-Int. Edit. 58 (2019) 9517-9521.

[80] J. Safaei, H. Ullah, N.A. Mohamed, M.F. Mohamad Noh, M.F. Soh, A.A. Tahir, N. Ahmad Ludin, M.A. Ibrahim, W.N.R. Wan Isahak, M.A. Mat Teridi, Appl. Catal. B: Environ. 234 (2018) 296-310.

[81] L. Liu, H. Huang, F. Chen, H. Yu, N. Tian, Y. Zhang, T. Zhang, Sci. Bull. 65 (2020) 934-943.

[82] Y. Yang, H. Chen, X. Zou, X.L. Shi, W.D. Liu, L. Feng, G. Suo, X. Hou, X. Ye, L. Zhang, C. Sun, H. Li, C. Wang, Z.G. Chen, ACS Appl. Mater. Interfaces 12 (2020) 24845-24854.

[83] Fang Li, Wei Zhao, D.Y.C. Leung, Appl. Catal. B: Environ. 258 (2019) 117954.

Table 1. Degradation rate constants (k_a) and relative coefficients (R^2) in decomposing RhB and phenol.

Catalyst	Pollutant	Degradation rate	k_a (min^{-1})	R^2
$BiVO_4$	RhB	13.6%	0.0143	0.8505
$Bi/BiVO_4$	RhB	80.9%	0.1979	0.9644
$BiVO_4$	Phenol	17.1%	0.031	0.9934
$Bi/BiVO_4$	Phenol	73.3%	0.2168	0.9817

Table 2. Resistance fitted according to the Nyquist plots of two samples.

Sample	$R_s \times 10^{-2}$ (Ω)	R_{ct} (Ω)	CPE$\times 10^{-6}$ (F)
$BiVO_4$	23.074	18.36	1.4565
$Bi/BiVO_4$	61.877	10.87	1.8762

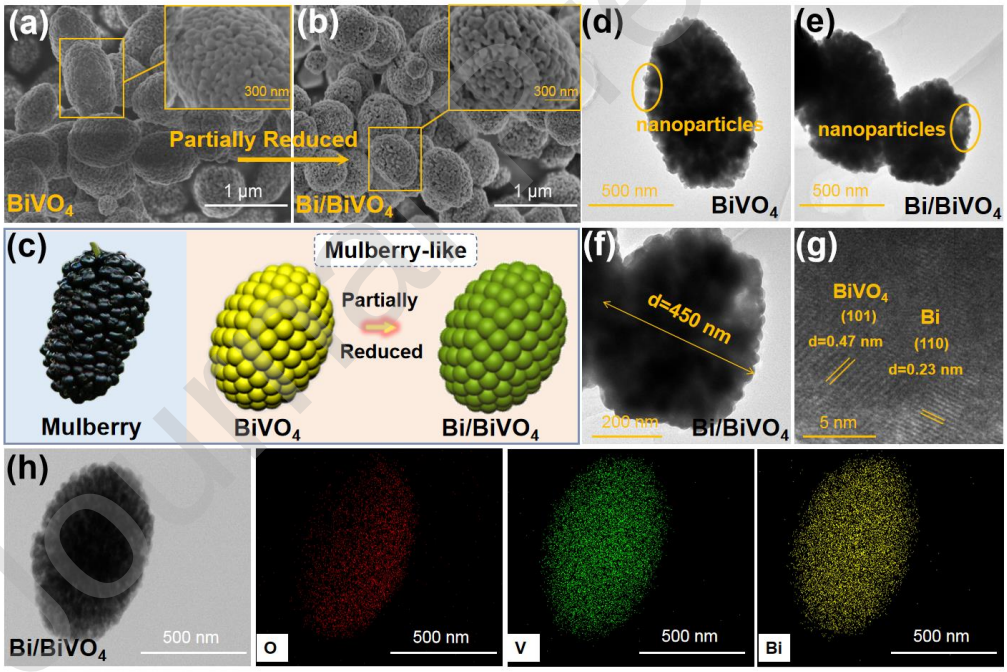

Fig. 1. SEM images of (a) $BiVO_4$ and (b) $Bi/BiVO_4$. (c) Schematic illustration for the morphology of the samples. (d-g) TEM images of $BiVO_4$ and $Bi/BiVO_4$. (h) EDS elemental mapping images of $Bi/BiVO_4$.

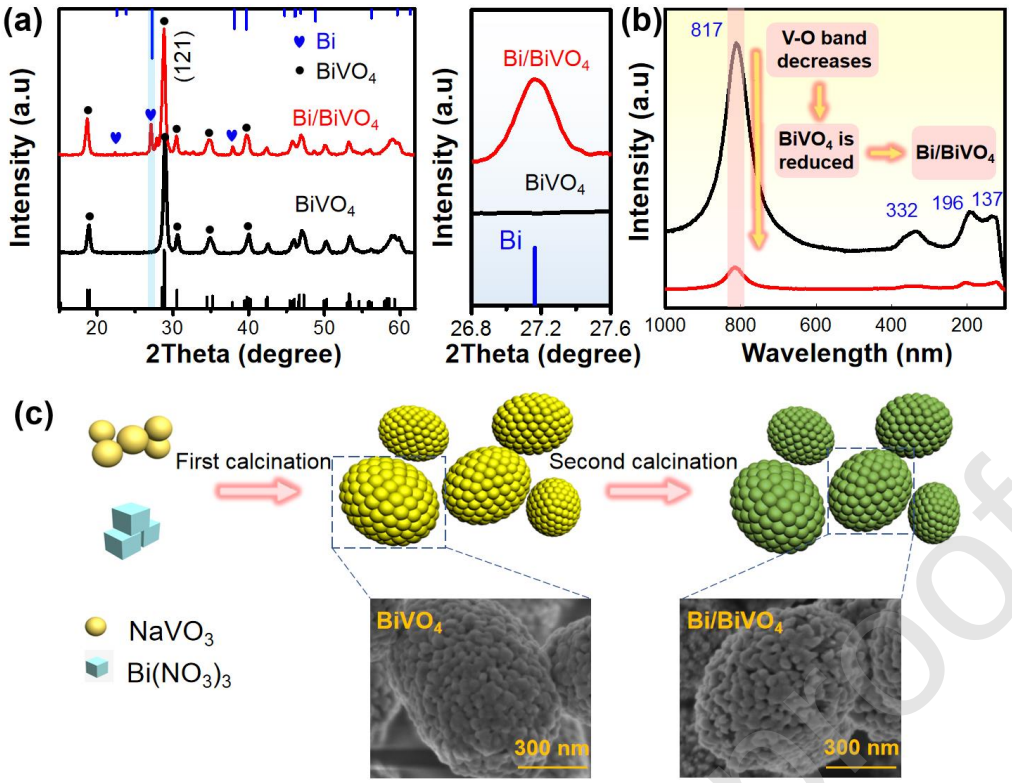

Fig. 2. (a) XRD patterns of the pure $BiVO_4$ and $Bi/BiVO_4$. (b) Raman spectra of $BiVO_4$ and $Bi/BiVO_4$. (c) Schematic illustration for the synthesis progress of the two-step calcination.

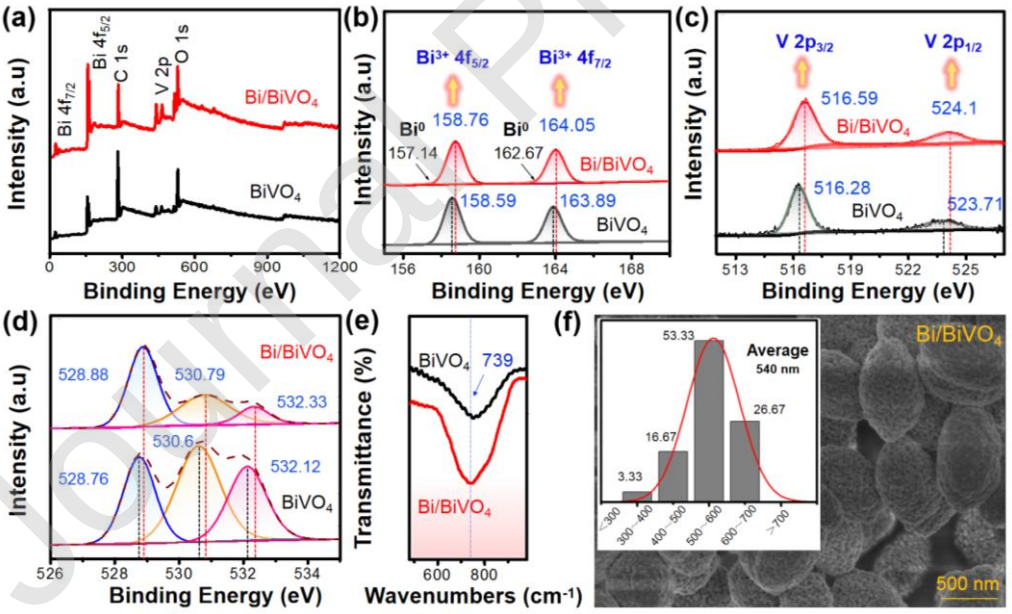

Fig. 3. (a) The entire XPS spectra of the pure $BiVO_4$ and $Bi/BiVO_4$. (b) Bi 4f, (c) V 2p and (d) O 1s for $BiVO_4$ and $Bi/BiVO_4$. (e) FTIR spectra of $BiVO_4$ and $Bi/BiVO_4$. (f) The

morphology of Bi/$BiVO_4$ and the corresponding diameter distribution of mulberry-like particles.

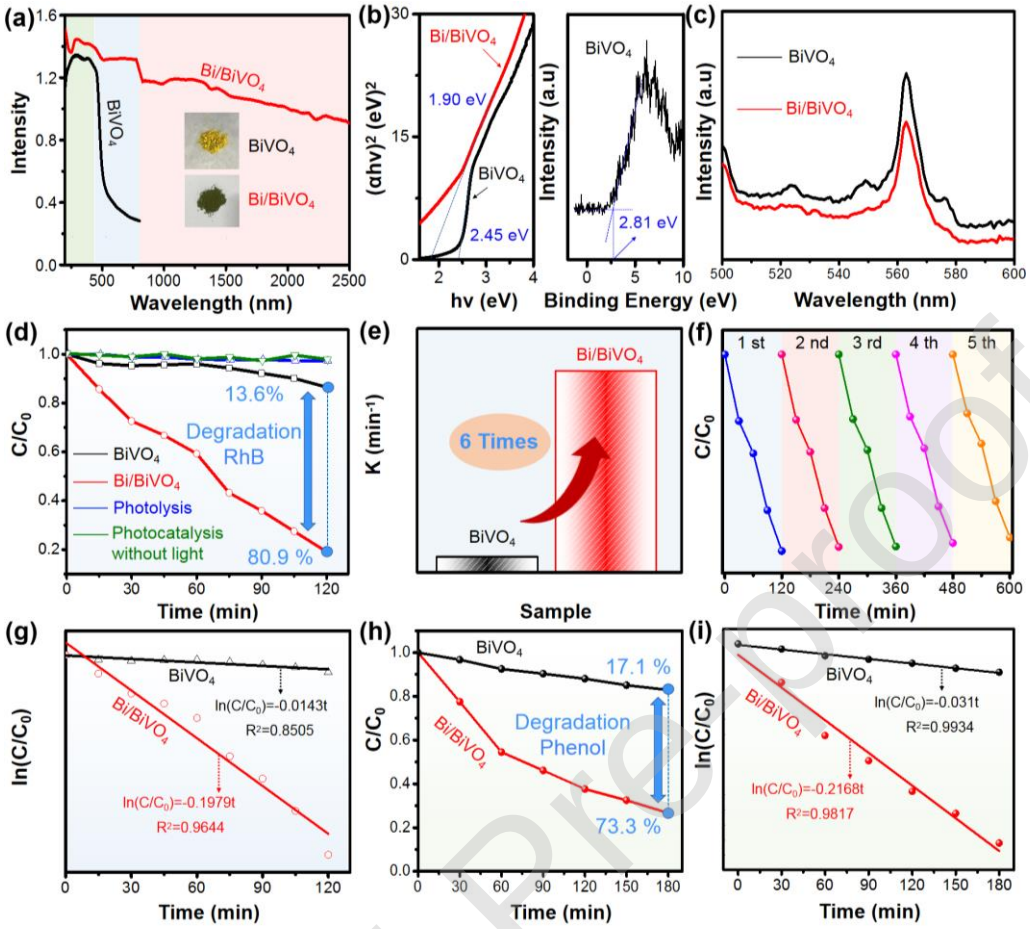

Fig. 4. (a) UV-vis absorption spectra and (b) bandgap and VB-XPS curves of $BiVO_4$ and Bi/$BiVO_4$. (c) PL spectra, (d, e) photocatalytic degradation of RhB, (f) cycling runs of Bi/$BiVO_4$ for the degradation of RhB and (g) the corresponding first-order plots of RhB photodegradation over $BiVO_4$ and Bi/$BiVO_4$. (h) Photocatalytic degradation and (i) the corresponding first-order plots of phenol photodegradation over $BiVO_4$ and Bi/$BiVO_4$.

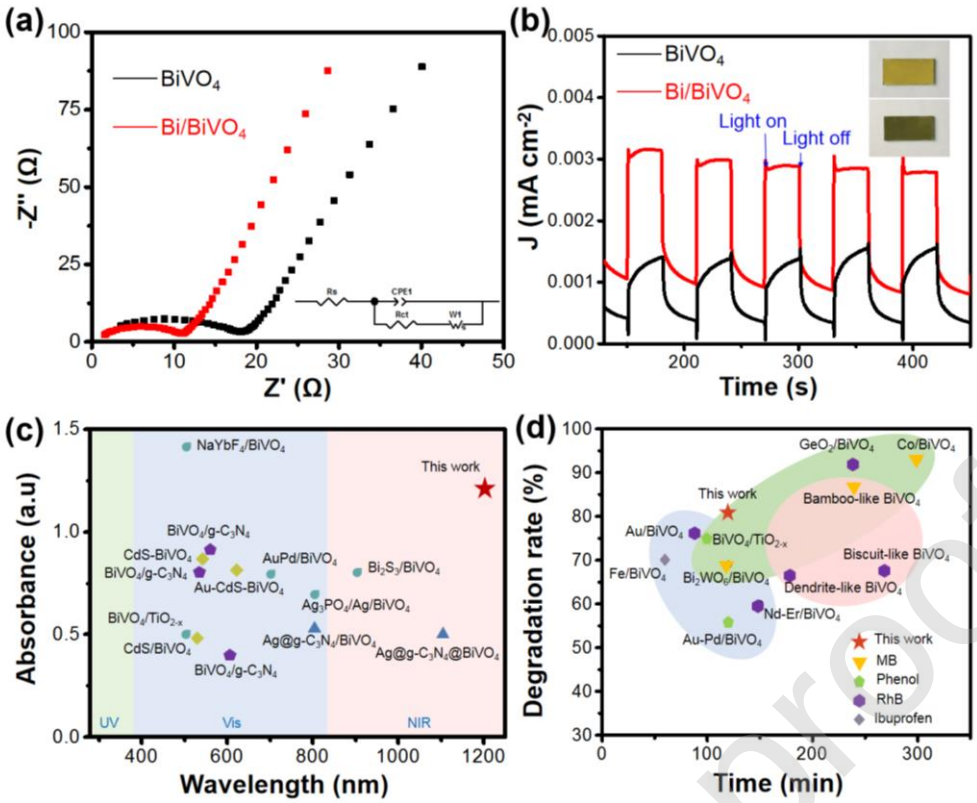

Fig. 5. (a) EIS Nyquist plot of the $BiVO_4$ and $Bi/BiVO_4$ electrodes measured in 0.1 M Na_2SO_4. (b) Photocurrent responses of as-prepared samples. Comparison of (c) light absorption range [13,17,44,57-65] and (d) degradation rate with reported values [66-73].

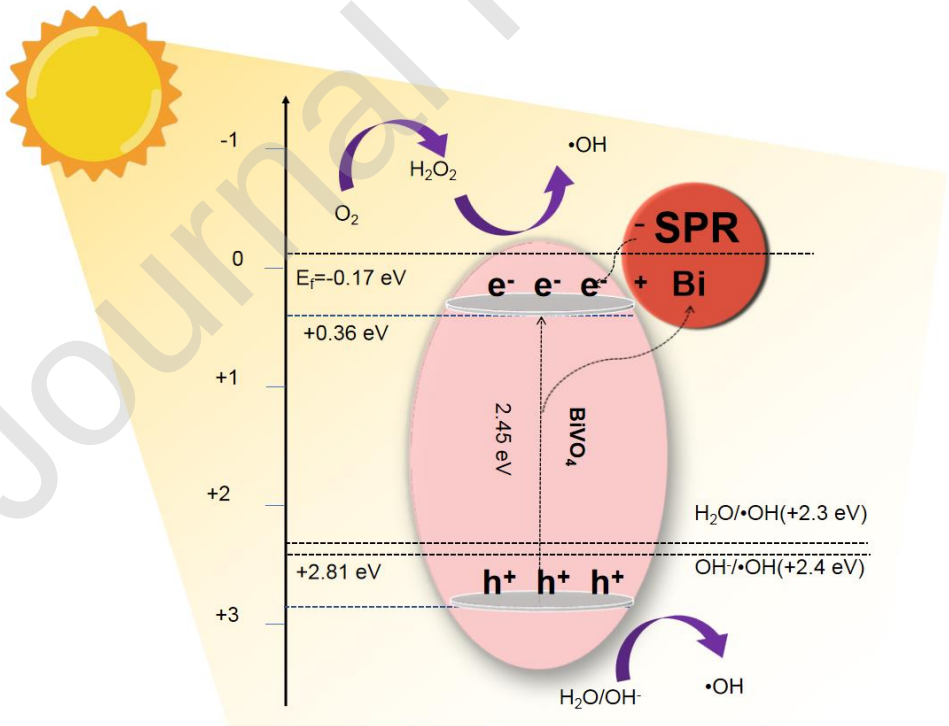

Fig. 6. Possible photocatalytic mechanism of the charge separation and transportation in Bi/$BiVO_4$.

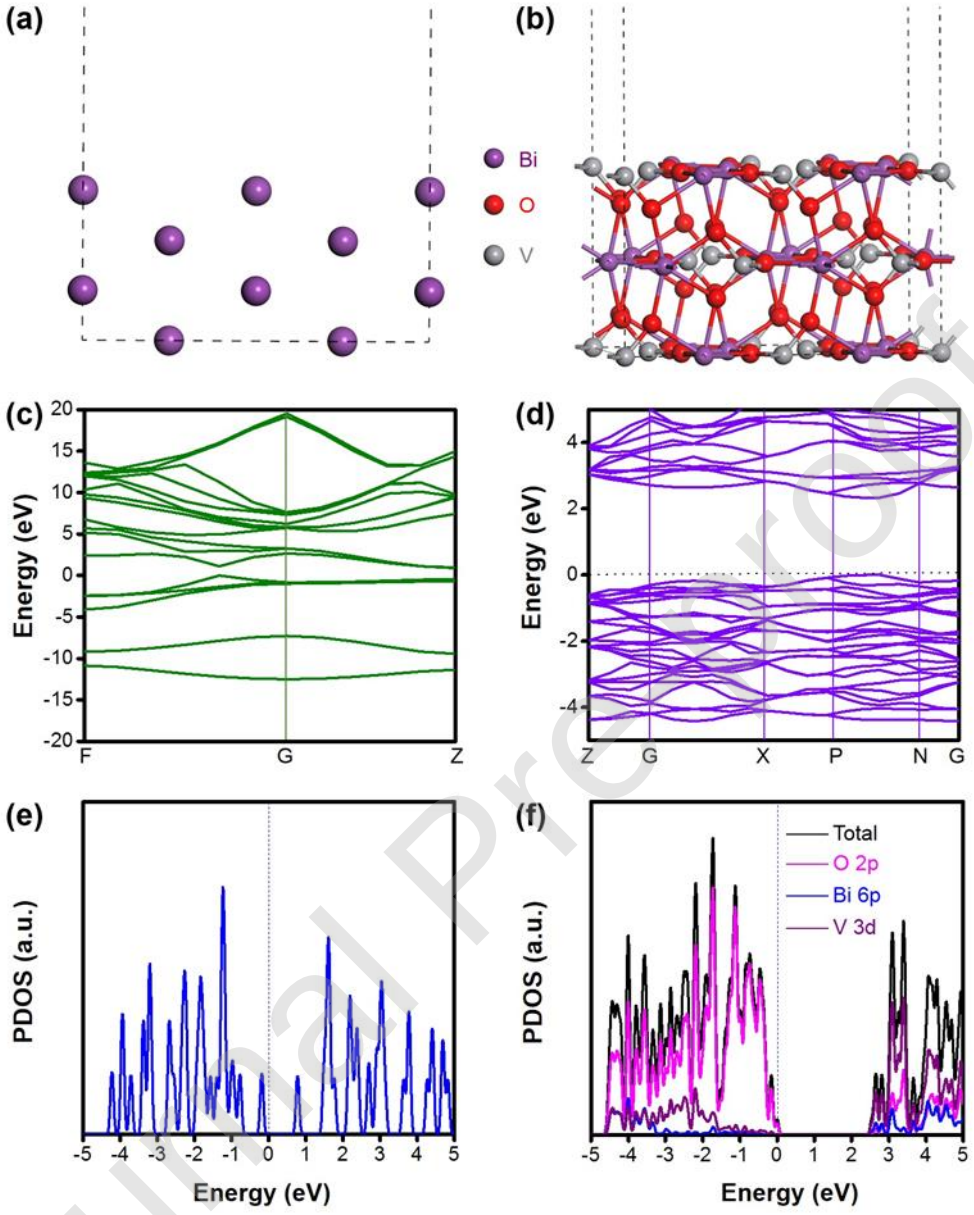

Fig. 7. Calculated structure of (a) Bi and (b) $BiVO_4$, the corresponding energy band of (c) Bi and (d) $BiVO_4$ and the corresponding PDOS of (e) Bi and (f) $BiVO_4$.

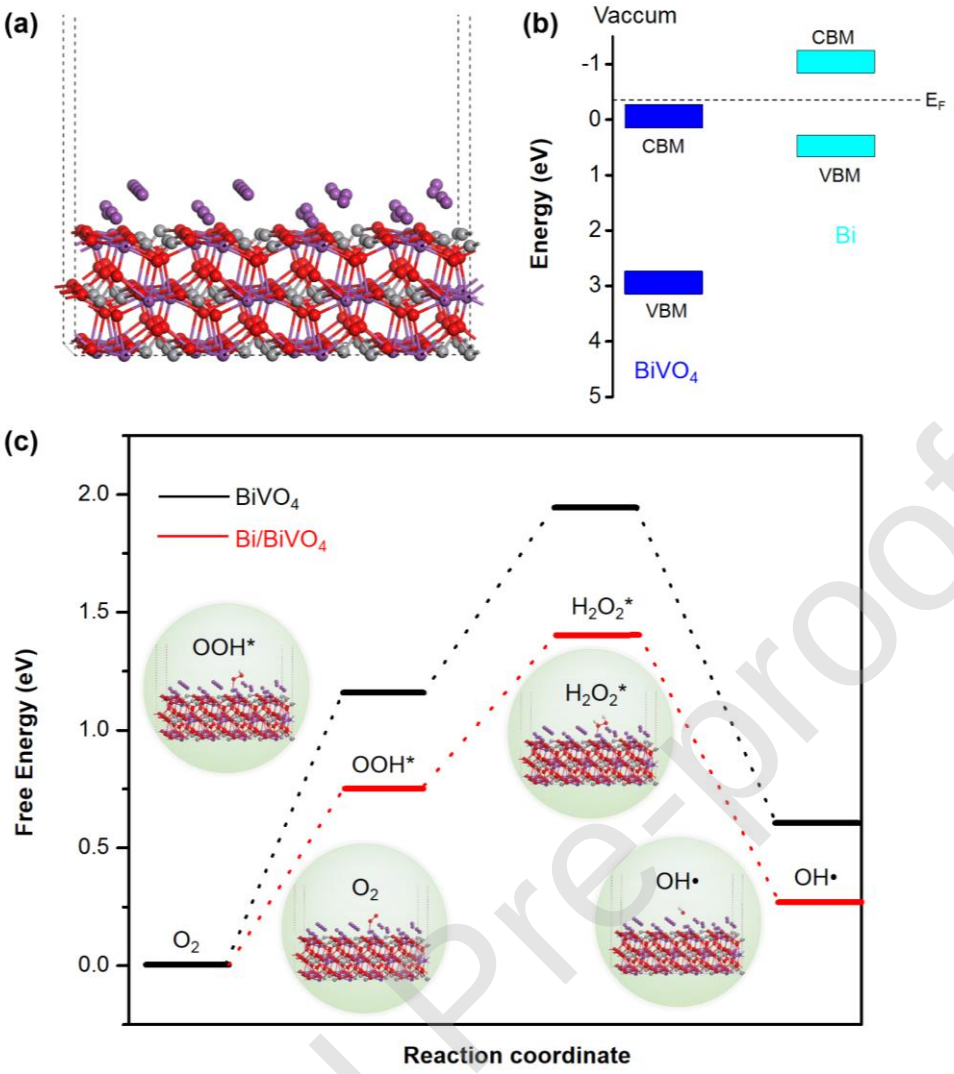

Fig. 8. (a) Calculated structure and (b) band position of $Bi/BiVO_4$. (c) The simulated free energy during the conversion from O_2 to •OH radicals of $Bi/BiVO_4$.